Alloyed Palladium-Silver Nanowires Stabilizing CO_2 Reduction to Formate

Na Han[1‡], Mingzi Sun[2‡], Yuan Zhou[1], Jie Xu[3], Chen Cheng[1], Rui Zhou[1], Liang Zhang[1], Jun Luo[3], Bolong Huang[2]* and Yanguang Li[1]*

[1]Institute of Functional Nano & Soft Materials (FUNSOM), Jiangsu Key Laboratory for Carbon-Based Functional Materials and Devices, Soochow University, Suzhou 215123, China

[2]Department of Applied Biology and Chemical Technology, The Hong Kong Polytechnic University, Hung Hom, Kowloon, Hong Kong SAR, China

[3]Center for Electron Microscopy and Tianjin Key Lab of Advanced Functional Porous Materials, Institute for New Energy Materials & Low-Carbon Technologies, School of Materials Science and Engineering, Tianjin University of Technology, Tianjin 300384, China

Correspondence to: bhuang@polyu.edu.hk; yanguang@suda.edu.cn

Abstract: Palladium can enable the electrochemical CO_2 reduction to formate with nearly zero overpotential and high selectivity. However, it usually suffers from the poor stability due to the CO poisoning from the intermediates of side reaction. Herein, we demonstrate that alloying palladium with silver is a promising strategy to significantly promote the electrocatalytic stability without sacrificing high CO_2 reduction selectivity and effiency. Palladium-silver (PdAg) alloy nanowires are prepared in aqueous solution with tunable chemical compositions, large aspect ratios and roughened surfaces. Both XPS and XANES characterizations indicated electron transfer from Ag to Pd upon alloying. Owing to the unique synergy effect between palladium and silver, the as-prepared nanowire exhibit excellent electrocatalytic performance for CO_2 reduction to formate. The best candidate Pd_4Ag nanowires enable the reaction at nearly zero overpotential, maintain high formate selectivity (>90%) until -0.3 V. Most impressively, most impressively, the superb long-term operation stability is achieved even at <-0.43 V

The remarkable stability resulted from the improved CO tolerance of Pd_4Ag nanowires during CO_2RR. In addition, DFT calculations confirmed that the incorporation of Ag in alloy nanowires downshifted the overall *d*-band center, and diluted the PdH_x active sites, which consequently weakened the CO binding on the Pd sites and improved the formate formation by selectively stabilizing the key intermediates. Our study here provides a viable solution to the long-standing stability issue associated with Pd-based materials and represent an advanced step towards their practical applications.

Electrochemical CO_2 reduction reaction (CO_2RR) converts CO_2 to renewable fuels and industrial building-block chemicals, which has been considered as a key step in the artificial carbon cycle.[1-3] By rationally tuning electrocatalyst materials and experimental conditions, a number of reduction products ranging from simple CO and formic acid to multi-carbon oxygenates and hydrocarbons.[3-9] Among them, the formic acid (or formate) is suggested to be one of the most commercially viable products by recent techoeconomic analyses.[10-12] Several p-block metals such as Sn, In and Bi are known to favor the formate production.[13-19] In particular, our group and other groups have successfully demonstrated that Bi can enable CO_2RR to formate with high selectivity close to 100% over a broad potential window.[20-26] Nevertheless, these p-block metals generally suffer from intermediate-to-large onset overpotentials ($\eta > 0.3$ V).[13] Compared to them, Pd is surprisingly unique, which reduces CO_2 to formate with nearly zero overpotential and high selectivity.[27-30] *Operando* spectroscopic characterizations support that the active species are PdH_x, which catalyzes CO_2RR presumably via a hydride-mediated pathway.[28, 31] Unfortunately, the great potential of Pd for the formate production is severely constrained by the high susceptibility to CO poisoning (as the side reaction intermediate), leading to the quick loss of electroactivity within hours and poor stability,

especially at potentials lower than -0.2 V versus reversible hydrogen electrode (RHE).[27, 32] Therefore, an increasing demand emerge for solutions to promote the CO tolerance of Pd electrocatalyst, and improve the operation stability for practical applications.

Alloying has beome a promising strategy to modulate electronic structure of Pd and the interactions with reaction intermediates. According to the *d*-band theory by Nørskov and coworkers,[33] alloying Pd with metals disaply the lower work functions, whichlower the *d*-band center and weaken the binding strength with key intermediates. Although such strategies have been applied as a general design principle of Pd-based alloys for electrocatalytic oxygen reduction reaction (ORR) and ethanol oxidation reaction (EOR),[34-37] the alloying effect is much less explored and appreciated for CO_2RR until very recently.[38-41] In this contribution, we investigate the great potential of one-dimensional (1D) PdAg alloy nanowires in CO_2RR electrocatalysis. Ag is selected as the second metal in the alloy for the electron-rich state and weak CO binding strength. We develop a facile solution method to prepare Pd-Ag alloy nanowires with a high aspect ratio and roughened surfaces. They enable selective and stable CO_2RR to formate even at <-0.4 V. Theoretical calculations indicate that the introduction of Ag significantly weakens CO adsorption on Pd and consequently improves the electrocatalytic stability for long-term applications.

1D Pd-Ag alloy nanowires were prepared from the co-reduction of H_2PdCl_4 and $AgNO_3$ in their aqueous solution by ascorbic acid with the presence of dihexadecyldimethylammonium chloride (DHDAC) as the structure-directing agent (see Experimental Method for details). The chemical composition of final products could be tuned over a wide range by simply adjusting the starting precursor ratio. They are denoted as Pd_xAg for the sake of clarity, where x indicates the nominal Pd/Ag molar ratio.

First, the crystal structure of the final product of Pd_4Ag are investigatedusing powder X-ray diffraction (XRD). As depicted in **Figure 1a**, Pd_4Ag exhibits diffraction peaks characteristic of the face-centered cubic structure. The separated peaks locate between those of pure Pd and Ag, which are relatively closer to the pristine Pd, evidencing the formation of a Pd-rich alloy according to the Vegard's law. Through the transmission electron microscopy (TEM) and scanning transmission electron microscopy (STEM), Pd_4Ag is unveiled to comprise of predominantly 1D nanowires with an average diameter of 5-6 nm and a length of several hundred nanometers (**Figure 1b-d**), together with a small fraction of nanoparticles. These nanowires are often curved, and some of them appear to be bundled or even melted together. The careful examination using aberration-corrected high-angle annular dark-field (HAADF) STEM reveals clear (111) and (200) lattice fringes (**Figure 1e**). Interestingly, we find that the nanowire surface is not atomically smooth but consists of a mixture of crystal facets including (111), (200), (211) and (311) as determined based on their crystallographic orientations. The nanowire diameter varies along the length, which seems to be originated from the imperfect merge and coalescence of nanoparticles. This leads us to believe that these 1D nanowires are formed from the oriented attachment of nanoparticles,[42] which also explains the co-presence of a small amount of nanoparticles in the final products. X-ray energy dispersive spectroscopy (EDS) elemental mapping of Pd and Ag along a single nanowire supports the uniform distribution of these two species (**Figure 1f**). Due to the proximity of Pd and Ag in the periodic table, the spatially distinguishment of these two elements at the atomic level using HAADF-STEM or electron energy loss spectroscopy (EELS) are not accessible. The inductively coupled plasma-atomic emission spectroscopy (ICP-AES) analysis of Pd_4Ag suggests that it is composed of 79.1 at% of Pd and 20.9 at% of Ag (**Table S1**), in good agreement with the starting Pd/Ag molar ratio. We find that when the

nominal Pd/Ag molar ratio is reduced from 4 to 2 or 1, the nanowire morphology can be approximately preserved (**Figure S1**). On the contrary, products of pure Pd or pure Ag from the same solution reaction mainly consist of nanoparticles. This is the first indication of the unique synergy between Pd and Ag. However,the underlying growth mechanism still needs the further exploration.

Furthermore, spectroscopic characterizations were carried out to probe the chemical state and the interaction between Pd and Ag in alloy nanowires. It is interesting to note that from X-ray photoelectron spectroscopy (XPS), the Pd 3d doublet of Pd_4Ag is displaced toward lower binding energy compared to pure Pd (**Figure 1g**), whereasthe Ag 3d doublet is displaced toward higher binding energy compared to pure Ag (**Figure 1h**). A similar trend is also garnered from X-ray absorption near edge structure (XANES) spectra at the Pd or Ag K-edge, which shows Pd in Pd_4Ag is slightly negatively charged ($Pd^{\delta-}$) and Ag is slightly positively charged ($Ag^{\varepsilon+}$) based on the shift of their adsorption edges (**Figure 1i-j**). The abovementioned data unambiguously confirm the electron transfer from Ag to Pd upon the alloying, which can be rationalized by the lower work function ofAgwith higher electron density than Pd.[43, 44] Meanwhile. the increasing electron filling of Pd *d* band is expected to lower the *d*-band center and alleviate the CO poisoning.

Next, we investigated the electrocatalytic performance of alloy nanowires in a standard H-cell, and compared them with pure Pd nanoparticles ~~side by side~~ (see Experimental Method for details). **Figure 2a** depicts the typical polarization curves of Pd_4Ag in N_2- or CO_2-saturated 0.1 M $KHCO_3$. These two curves start to diverge at ~0 V (versus RHE), which signals the CO_2RR onset potential and is close to the theoretical value of CO_2RR to formate (-0.017 V). The cathodic current density is approximately doubled in the presence of CO_2.

In order to quantify the potential-dependent formate selectivity, electrocatalysts were biased at a

few selected potentials between 0 and -0.45 V. The amount of formate produced was measured using ion chromatography at the end of each electrolysis. A comparison between Pd and Pd_4Ag immediately discloses a striking difference. The chronoamperometric ($i \sim t$) curves of pure Pd start to decline once the working potential approaches or goes beyond -0.1 V owing to the severe CO poisoning, in line with previous reports (**Figure S2**).[28-30, 32, 45] The degradation is further aggravated with increasing overpotential: at -0.39 V, the cathodic current density quickly drops from 5 mA cm^{-2} to 2.2 mA cm^{-2} after 1 h electrolysis. Product analysis indicates the Faradaic efficiency of formate is 65% at ~0 V, which then gradually raises to 94% at -0.23 V and drops again to 57% at -0.38 V (**Figure 2c**). By contrast, the chronoamperometric curves of Pd_4Ag nanowires show the absence of subtle sign of the deactivation of electrocatalyst even at a relatively negative potential of -0.44 V (**Figure 2b**). The formate Faradaic efficiency of Pd_4Ag is measured to be 90% at ~0 V, and remains >95% between -0.08 V to -0.24 V (**Figure 2c**). An efficiency of 67% is still retained at -0.44 V — a potential known to generally favor hydrogen evolution reaction (HER) over CO_2RR. We also evaluate Pd_2Ag and PdAg nanowires which have slightly inferior stability and formate selectivity compared to those of Pd_4Ag. However, when compare to Pd, these alloys still show significantly improved performances than the pristine Pd nanoparticles (**Figure S3**).

In addition, it is of critical importance to assess the long-term working stability of alloy nanowires since increasing CO accumulation on the Pd surface is more likely to seriously impact the electrocatalyst over the long run. In our knowledge, there have been very few demonstrations about the long-term stability of Pd-based electrocatalysts for CO_2RR to formate at <-0.3 V. Not surprisingly, we find that the cathodic current density of pure Pd is subjected to a rapid decay within the first 2000 s when biased at -0.24 V or -0.38 V, and finally levels off at <1 mA cm^{-2} (**Figure 2d**). Pd_4Ag enables

superb operation stability at the investigated potential of -0.25 V, -0.34 V or -0.43 V. The current density only slightly decreases from 6.0 mA cm^{-2} to 5.8 mA cm^{-2} after 15000 s electrolysis at -0.43 V. The average formate Faradaic efficiency is measured to be 97%, 88% and 69% at -0.26 V, -0.34 V and -0.42 V, respectively, which is consistent with Figure 2c and indicates no loss of selectivity as well during the long-term operation. The combination of improved formate selectivity and remarkable stability even at intermediate overpotentials (where it is formate stably produced on Pd) renders our electrolysts superior to other Pd-based CO_2RR materials.[30, 32, 40, 45-50] It again highlights the advantageous synergy between Pd and Ag in alloy nanowires.

We propose that the outstanding electrocatalytic performance observed is a direct consequence of the improved CO tolerance of alloy nanowires. The electrochemical experiments were designed to confirm our hypothesis. CO stripping voltammetry of Pd_4Ag and pure Pd were first conducted and compared in 1 M KOH. As we can see from **Figure S4**, pure Pd exhibits a sharp CO oxidation peak centered at 0.74 V, whereas the CO oxidation peak of Pd_4Ag is negatively shifted ~200 mV and becomes centered at 0.56 V. This clearly infers the weaker CO binding on the alloy than the pristine Pd. It should be noted that CO stripping voltammetry was carried out in 1 M KOH instead of 0.1 M $KHCO_3$ because catalysts had much better resolved CO oxidation peaks in KOH (as Figure 3a,b). Nevertheless, the conclusion about weakened CO adsorption is intrinsic to Pd_4Ag and should also apply during CO_2RR in 0.1 M $KHCO_3$. ….TPD….

In order to directly quantify the amount of CO accumulation on the catalyst surface during CO_2RR, Pd_4Ag and Pd were biased at different working potentials for 1 h in 0.1 M $KHCO_3$, and then immediately subjected to positive sweeps from their working potential up to 0.9~1.0 V (**Figure 3a,b**). The peak area corresponding to CO oxidation was integrated and plotted against CO_2RR working

potential for both samples in **Figure 3c**. We find that 1 h CO_2RR electrolysis at -0.15 V on pure Pd leads to CO accumulation of 59 mC cm^{-2} on the surface, which quickly increases with the overpotential and reaches 177 mC cm^{-2} at -0.32 V. Very impressively, the amount of CO accumulation on Pd_4Ag is 2-3 times less: only 82 mC cm^{-2} is measured even after the electrocatalyst is biased at -0.44 V for 1 h.

As a step further, density functional theory (DFT) calculations were conducted to understand the improved electrocatalytic performance from the theoretical aspect. lattice structure of Pd_4Ag has demonstrated high stability with very limited distortion of atomic arrangements even after the introduction of Ag, which is ascribed to a similar atomic radius between Pd and Ag. Meanwhile, with the introduction of Ag, the surface electronic distribution has been strongly interrupted when compared to the pure Pd surface. The antibonding and bonding orbitals near the Fermi level are dominated by the Pt sites, where the doped Ag modulates the electroactivity of the surface for CO_2RR (**Figure 4a,b**). To unravel the electronic structure of Pd_4Ag, the projected partial density of states (PDOS) has been demonstrated to compare with pristine Pd. Notably, the Ag-4d orbitals display the evident electron-rich feature since the dominant peak of d-orbital locates on E_V-4.77 eV (E_V = 0 eV)., which may serve as the electron reservoir and supply electrons to Pd. This is consistent with the electron transfer from Ag to Pd experimentally concluded based on XPS and XANES results. Pd-4d orbitals in Pd_4Ag have been modulated, in which the explicit peak splitting in the Pd metal is the absence in the PdAg. Alloying Pd with Ag causes the overall *d*-band center to downshift due to the deep position of Ag 4*d* orbitals, and therefore is expected to weaken the binding toward the CO intermediate (**Figure 4c**). The site-dependent electronic structure is also highly crucial for our understanding of improved CO_2RR performance. From the bulk to the surface, the Pd-4d orbitals have shown a gradual expansion, which facilitates the site-to-site electron transfer on the surfaces. Moreover, although the Pd-4d becomes

broader on the surface, the dominant peaks become more concentrated near the E_F, leading to an enhanced selectivity (**Figure 4d**). The Ag-4d bands demonstrate the gradual upshifting trend from the bulk to the surface, supporting the improved coupling with neighboring Pd to guarantee the efficient site-to-site electron transfer (**Figure 4e**). Upon the initial adsorption, the *s*,*p* orbitals of CO_2 downshifts, signaling the electron transfer from the catalyst surface to CO_2 that stabilizes the adsorbate (**Figure 4f**). The stronger linear correlation in the electronic structure of p-σ components of the intermediates guarantees the efficient electron transfer between each reaction coordinates. Notably, a linear correlation from *CO_2 to the final product *HCOOH is observed, which supports an efficient electron transfer during the CO_2RR to produce formate.

Then, we further investigate the structural configuration of the stabilized adsorbates during the CO_2RR. The adsorption of both CO_2 and CO still locates near the Pd sites, where the introduction of Ag leads to a distinct adsorption trend. For the key adsorbates HCOO* and final product formate, the Ag sites show more favorable adsorption, supporting the pivotal role of Ag in stabilizing the intermediates without overbinding (**Figure 4g**) In addition, the energetic reaction pathway and the binding energies comparison have been demonstrated. For the formation of formate by CO_2, the key reaction is the first hydrogenation of the reaction from CO_2 to HCOO*. In comparison, the formation of COOH* results in the formation of CO with lowered formate selectivity. Notably, the initial hydrogenation of the binding display distinct selectivity, in which the binding between H and C is much more favorable with an energy barrier of 1.15 eV. The final formation of formate shows an energy release of 0.99 eV, which also avoids the overbinding effect to reduce CO_2RR efficiency. On the contrary, the formation of CO is an endothermic reaction, requiring an energy barrier of 0.32 eV (**Figure 4h**). Moreover, the binding strength of CO and CO_2 is significant to determine the efficiency

and stability in long-term applications. For the initial CO_2 binding, the Pd_4Ag has shown much lower binding energies than the pristine Pd catalyst. This evident difference indicates the essential advantage of PdAg in CO_2RR. For the CO binding, Pd has been proved with a strong binding trend, which is also consistent with our results. After the introduction of Ag, the CO binding energies have significantly increased, which supports the improved resistance of the CO poisoning. The improved performance is attributed to the separation of highly electroactive Pd sites to optimize the binding and electron transfer for CO_2RR (**Figure 4i**). For the PdH_x, the surface activated Pd sites by adsorbed H leads to a strong binding preference to both CO_2 and CO, which results in the inevitable stability issue due to the CO poisoning. With the introduced Ag on the surface, PdAg demonstrates a different mechanism with improved resistance to the CO poisoning, which is attributed to the less PdH_x site assembly. The introduction of Ag sites has separated the PdH_x sites, where the neighboring effect between these active sites becomes much weaker with a reduced binding trend to CO. Meanwhile, the Ag sites are able to stabilize the intermediates of CO_2RR due to the coupling with neighboring Pd sites, which further promotes the electrocatalysis. Due to the increased isolated PdH_x sites, the overbinding effect has also been significantly suppressed to guarantee the efficient desorption of formate. Therefore, the synergistic effect of Pd and Ag sites contribute to the significantly improved selectivity and stability of CO_2RR to generate formate (**Figure 4j**).

In conclusion, we explored the alloying effect between Pd and Ag for promoting CO_2RR to formate. Pd_xAg nanowires were prepared via a facile solution method in the presence of DHDAC. The final products featured tunable chemical compositions, long aspect ratio and roughened surfaces. Both XPS and XANES characterizations indicated electron transfer from Ag to Pd upon alloying. These alloy nanowires exhibited great electrocatalytic performances for CO_2RR to formate in 0.1 M $KHCO_3$.

The best candidate - Pd_4Ag nanowires could enable the reaction at nearly zero overpotential, maintain high formate selectivity (>90%) until -0.3 V, and most impressively, demonstrate superb long-term operation stability even at <-0.43 V where people previously believed that formate could not be stably produced on Pd. The remarkable stability was resulted from the improved CO tolerance of Pd_4Ag nanowires as evidenced by CO stripping voltammetry and detailed analysis of their potential-dependent CO surface coverage during CO_2RR. In addition, DFT calculations have confirmed the enhanced CO_2RR performances of PdAg originate from the modified binding strength with reactants and intermediates. The introduced electron-rich Ag sites play as the electron-reservoir to stabilize the intermediates and promote the site-to-site electron transfer, which significantly suppresses the CO binding and improves the formation of formate.. Our study here provides a viable solution to the long-standing stability issue associated with Pd-based materials, and may represent an important step toward their practical applications.

Acknowledgements

We acknowledge the support from the Ministry of Science and Technology of China (2017YFA0204800 and 2017YFA0700104), the National Natural Science Foundation of China (2190020225 and 51825102, 21771156), Tianjin Science Fund for Distinguished Young Scholars (19JCJQJC61800), the Priority Academic Program Development of Jiangsu Higher Education Institutions and Collaborative Innovation Center of Suzhou Nano Science and Technology. XAS measurements were carried out at beamline 44A at Taiwan Photon Source (TPS).

Conflict of Interest

The authors declare no conflict of interest.

References

[1] C. Hepburn, E. Adlen, J. Beddington, E. A. Carter, S. Fuss, N. Mac Dowell, J. C. Minx, P. Smith, C. K. Williams, *Nature* **2019**, *575*, 87.

[2] Y. Y. Birdja, E. Perez-Gallent, M. C. Figueiredo, A. J. Gottle, F. Calle-Vallejo, M. T. M. Koper, *Nat. Energy* **2019**, *4*, 732.

[3] M. B. Ross, P. De Luna, Y. Li, C. T. Dinh, D. Kim, P. Yang, E. H. Sargent, *Nat. Catal.* **2019**, *2*, 648.

[4] D. T. Whipple, P. J. A. Kenis, *J. Phys. Chem. Lett.* **2010**, *1*, 3451.

[5] D. Gao, R. M. Aran-Ais, H. S. Jeon, B. Roldan Cuenya, *Nat. Catal.* **2019**, *2*, 198.

[6] M. G. Kibria, J. P. Edwards, C. M. Gabardo, C. T. Dinh, A. Seifitokaldani, D. Sinton, E. H. Sargent, *Adv. Mater.* **2019**, *31*, 1807166.

[7] L. Li, Y. Huang, Y. Li, *EnergyChem* **2020**, *2*, 100024.

[8] F. Lv, N. Han, Y. Qiu, X. Liu, J. Luo, Y. Li, *Coordin. Chem. Rev.* **2020**, *422*, 213435.

[9] L. Fan, C. Xia, F. Yang, J. Wang, H. Wang, Y. Lu, *Sci. Adv.* **2020**, *6*, eaay3111.

[10] O. S. Bushuyev, P. De Luna, C. T. Dinh, L. Tao, G. Saur, J. van de Lagemaat, S. O. Kelley, E. H. Sargent, *Joule* **2018**, *2*, 825.

[11] M. Jouny, W. Luc, F. Jiao, *Ind. Eng. Chem. Res.* **2018**, *57*, 2165.

[12] J. M. Spurgeon, B. Kumar, *Energy Environ. Sci.* **2018**, *11*, 1536.

[13] N. Han, P. Ding, L. He, Y. Li, Y. Li, *Adv. Energy Mater.* **2020**, *10*, 1902338.

[14] H. Yang, Y. Huang, J. Deng, Y. Wu, N. Han, C. Zha, L. Li, Y. Li, *J. Energy Chem.* **2019**, *37*, 93.

[15] F. Lei, W. Liu, Y. Sun, J. Xu, K. Liu, L. Liang, T. Yao, B. Pan, S. Wei, Y. Xie, *Nat. Commun.* **2016**, *7*, 12697.

[16] X. Zheng, P. De Luna, F. P. G. de Arquer, B. Zhang, N. Becknell, M. B. Ross, Y. Li, M. N. Banis, Y. Li, M. Liu, *Joule* **2017**, *1*, 794.

[17] N. Han, Y. Wang, J. Deng, J. Zhou, Y. Wu, H. Yang, P. Ding, Y. Li, *J. Mater. Chem. A* **2019**, *7*, 1267.

[18] R. Zhou, N. Han, Y. Li, *J. Electrochem.* **2019**, *25*, 445.

[19] W. Ma, S. Xie, X. Zhang, F. Sun, J. Kang, Z. Jiang, Q. Zhang, D. Wu, Y. Wang, *Nat. Commun.* **2019**, *10*, 892.

[20] Q. Gong, P. Ding, M. Xu, X. Zhu, M. Wang, J. Deng, Q. Ma, N. Han, Y. Zhu, J. Lu, *Nat. Commun.* **2019**, *10*, 2807.

[21] H. Yang, N. Han, J. Deng, J. Wu, Y. Wang, Y. Hu, P. Ding, Y. Li, Y. Li, J. Lu, *Adv. Energy Mater.* **2018**, *8*, 1801536.

[22] N. Han, Y. Wang, H. Yang, J. Deng, J. Wu, Y. Li, Y. Li, *Nat. Commun.* **2018**, *9*, 1320.

[23] P. Ding, Y. Hu, J. Deng, J. Chen, C. Zha, H. Yang, N. Han, Q. Gong, L. Li, T. Wang, *Mater. Today Chem.* **2019**, *11*, 80.

[24] L. Fan, C. Xia, P. Zhu, Y. Lu, H. Wang, *Nat. Commun.* **2020**, *11*, 3633.

[25] C. Xia, P. Zhu, Q. Jiang, Y. Pan, W. Liang, E. Stavitsk, H. N. Alshareef, H. Wang, *Nat. Energy* **2019**, *4*, 776.

[26] C. W. Lee, J. S. Hong, K. D. Yang, K. Jin, J. H. Lee, H. Y. Ahn, H. Seo, N. E. Sung, K. T. Nam, *ACS Catal.* **2018**, *8*, 931.

[27] D. Gao, H. Zhou, F. Cai, J. Wang, G. Wang, X. Bao, *ACS Catal.* **2018**, *8*, 1510.

[28] D. Gao, H. Zhou, F. Cai, D. Wang, Y. Hu, B. Jiang, W. Cai, X. Chen, R. Si, F. Yang, S. Miao, J. Wang, G. Wang, X. Bao, *Nano Res.* **2017**, *10*, 2181.

[29] A. Klinkova, P. De Luna, C. T. Dinh, O. Voznyy, E. M. Larin, E. Kumacheva, E. H. Sargent, *ACS Catal.* **2016**, *6*,

8115.
[30] F. Cai, D. Gao, H. Zhou, G. Wang, T. He, H. Gong, S. Miao, F. Yang, J. Wang, X. Bao, *Chem. Sci.* **2017**, *8*, 2569.
[31] W. Sheng, S. Kattel, S. Yao, B. Yan, Z. Liang, C. J. Hawxhurst, Q. Wu, J. G. Chen, *Energy Environ. Sci.* **2017**, *10*, 1180.
[32] X. Min, M. W. Kanan, *J. Am. Chem. Soc.* **2015**, *137*, 4701.
[33] B. Hammer, J. K. Nørskov, *Adv. Catal.* **2000**, *45*, 71.
[34] C. Zhu, S. Guo, S. Dong, *Adv. Mater.* **2012**, *24*, 2326.
[35] L. Zhang, Q. Chang, H. Chen, M. Shao, *Nano Energy* **2016**, *29*, 198.
[36] W. Huang, X. Kang, C. Xu, J. Zhou, J. Deng, Y. Li, S. Cheng, *Adv. Mater.* **2018**, *30*, 1706962.
[37] S. R. Chowdhury, S. Ghosh, S. K. Bhattachrya, *Electrochim. Acta* **2017**, *225*, 310.
[38] S. Chatterjee, C. Griego, J. L. Hart, Y. Li, M. L. Taheri, J. Keith, J. D. Snyder, *ACS Catal.* **2019**, *9*, 5290.
[39] Y. Zhou, R. Zhou, X. Zhu, N. Han, B. Song, T. Liu, G. Hu, Y. Li, J. Lu, Y. Li, *Adv. Mater.* **2020**, *32*, 2000992.
[40] R. Kortlever, I. Peters, S. Koper, M. T. M. Koper, *ACS Catal.* **2015**, *5*, 3916.
[41] X. Bai, W. Chen, C. Zhao, S. Li, Y. Song, R. Ge, W. Wei, Y. Sun, *Angew. Chem. Int. Ed.* **2017**, *129*, 12387.
[42] Q. Zhang, S. Liu, S. Yu, *J. Mater. Chem.* **2009**, *19*, 191.
[43] P. Verma, Y. Kuwahara, K. Mori, H. Yamashita, *J. Mater. Chem. A* **2016**, *4*, 10142.
[44] W. He, X. Li, Z. Qian, Z. Liu, Z. Tang, *Int. J. Electrochem. Sci.* **2019**, *14*, 8781.
[45] F. Zhou, H. Li, M. Fournier, D. R. MacFarlane, *ChemSusChem* **2017**, *10*, 1509.
[46] B. Jiang, X. Zhang, K. Jiang, D. Wu, W. Cai, *J. Am. Chem. Soc.* **2018**, *140*, 2880.
[47] C. Zhao, Z. Yin, J. Wang, *ChemElectroChem* **2015**, *2*, 1974.
[48] Y. Hou, R. Erni, R. Widmer, M. Rahaman, H. Guo, R. Fasel, P. Moreno‐García, Y. Zhang, P. Broekmann, *ChemElectroChem* **2019**, *6*, 3189.
[49] T. Takashima, T. Suzuki, H. Irie, *Electrochim. Acta* **2017**, *229*, 415.
[50] R. Kortlever, C. Balemans, Y. Kwon, M. T. M. Koper, *Catal. Today* **2015**, *244*, 58.

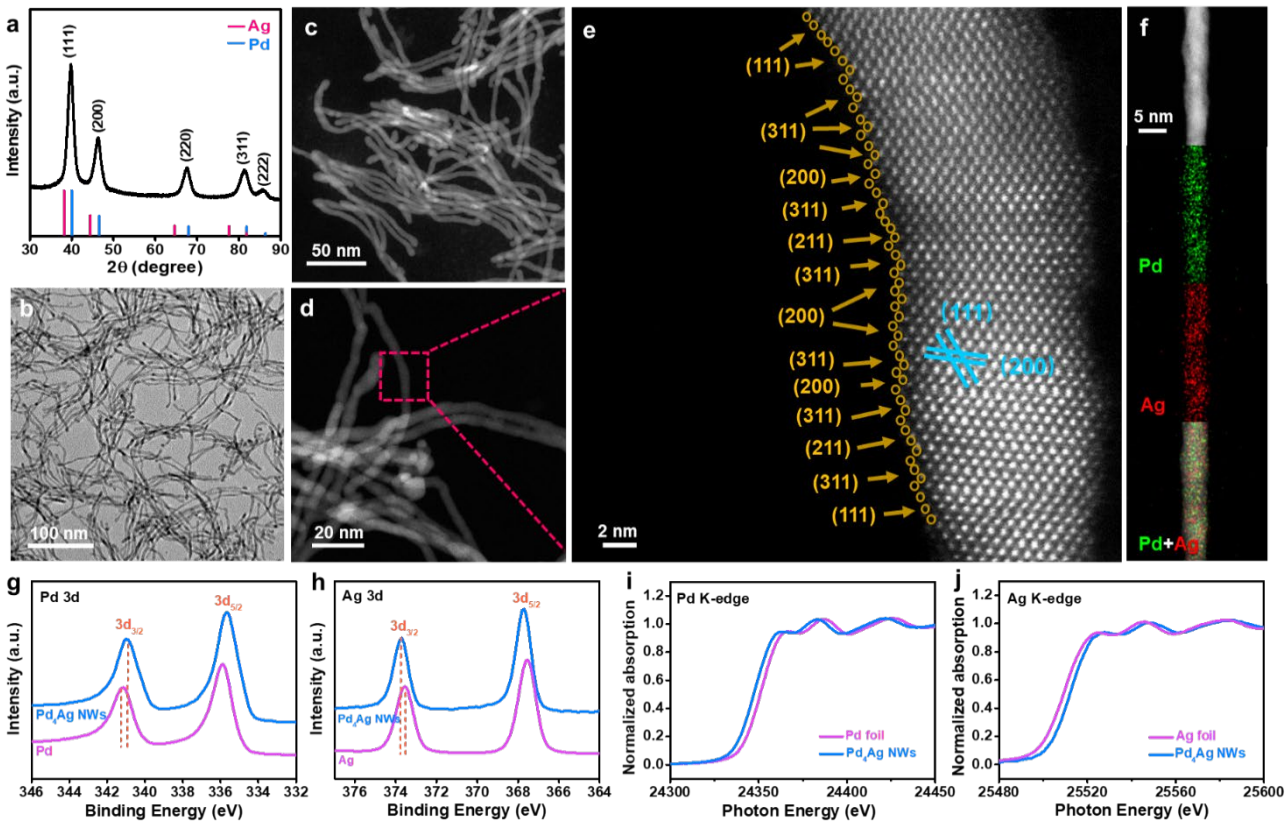

Figure 1. Structural characterizations of Pd_4Ag nanowires. (a) XRD pattern, (b) TEM image and (c, d) STEM images of Pd_4Ag nanowires; (e) aberration-corrected HAADF-STEM image of a Pd_4Ag nanowire from the enclosed region in (d); (f) STEM image and corresponding EDS elemental mapping of a Pd_4Ag nanowire; (g) Pd 3d XPS spectra of Pd_4Ag and pure Pd; (h) Ag 3d XPS spectra of Pd_4Ag and pure Ag; (i) Pd K-edge XANES of Pd_4Ag and the Pd reference; (j) Ag K-edge XANES spectra of Pd_4Ag and the Ag reference.

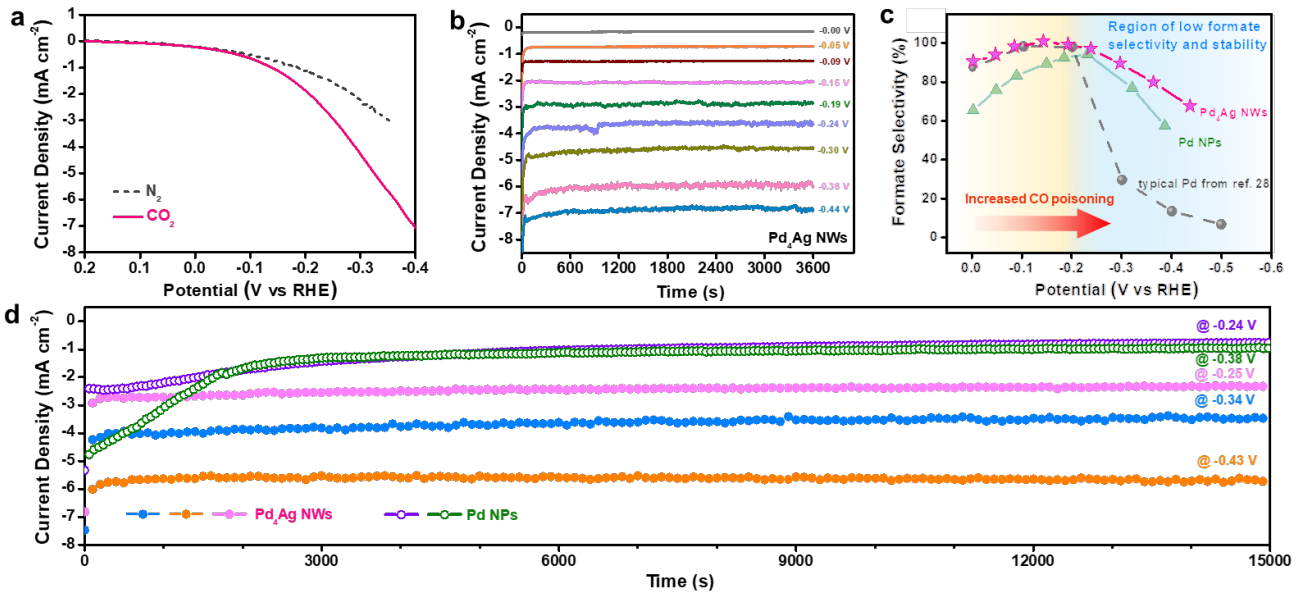

Figure 2. CO_2RR performance of Pd_4Ag nanowires in 0.1 M $KHCO_3$. (a) Polarization curves of Pd_4Ag in CO_2- or N_2-saturated electrolyte; (b) total current density of Pd_4Ag at different working potentials as indicated; (c) potential-dependent formate selectivity of Pd_4Ag in comparison with those of pure Pd and typical Pd catalyst from the literature; (d) long-term chronoamperometric curves of Pd_4Ag and pure Pd for 15000 s at a few selected potentials as indicated.

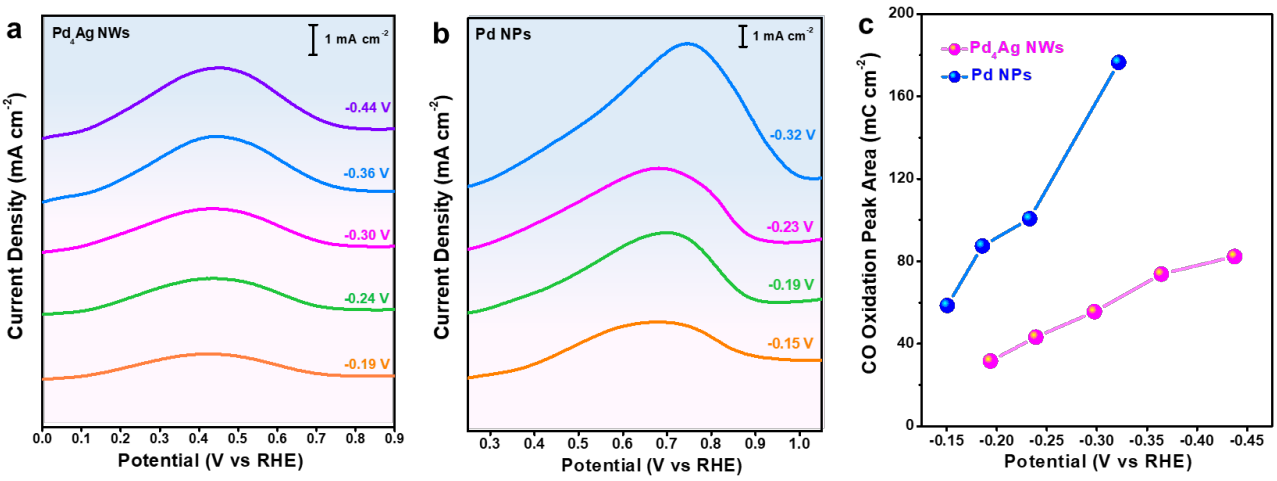

Figure 3. Analysis of the CO accumulation on Pd_4Ag and pure Pd during CO_2RR. (a, b) Positive going polarization curves on (a) Pd_4Ag and (b) pure Pd immediately after 1 h CO_2RR electrocatalysis at different working potentials; (c) intergrated peak areas for the CO oxidation on Pd_4Ag and pure Pd at different working potentials.

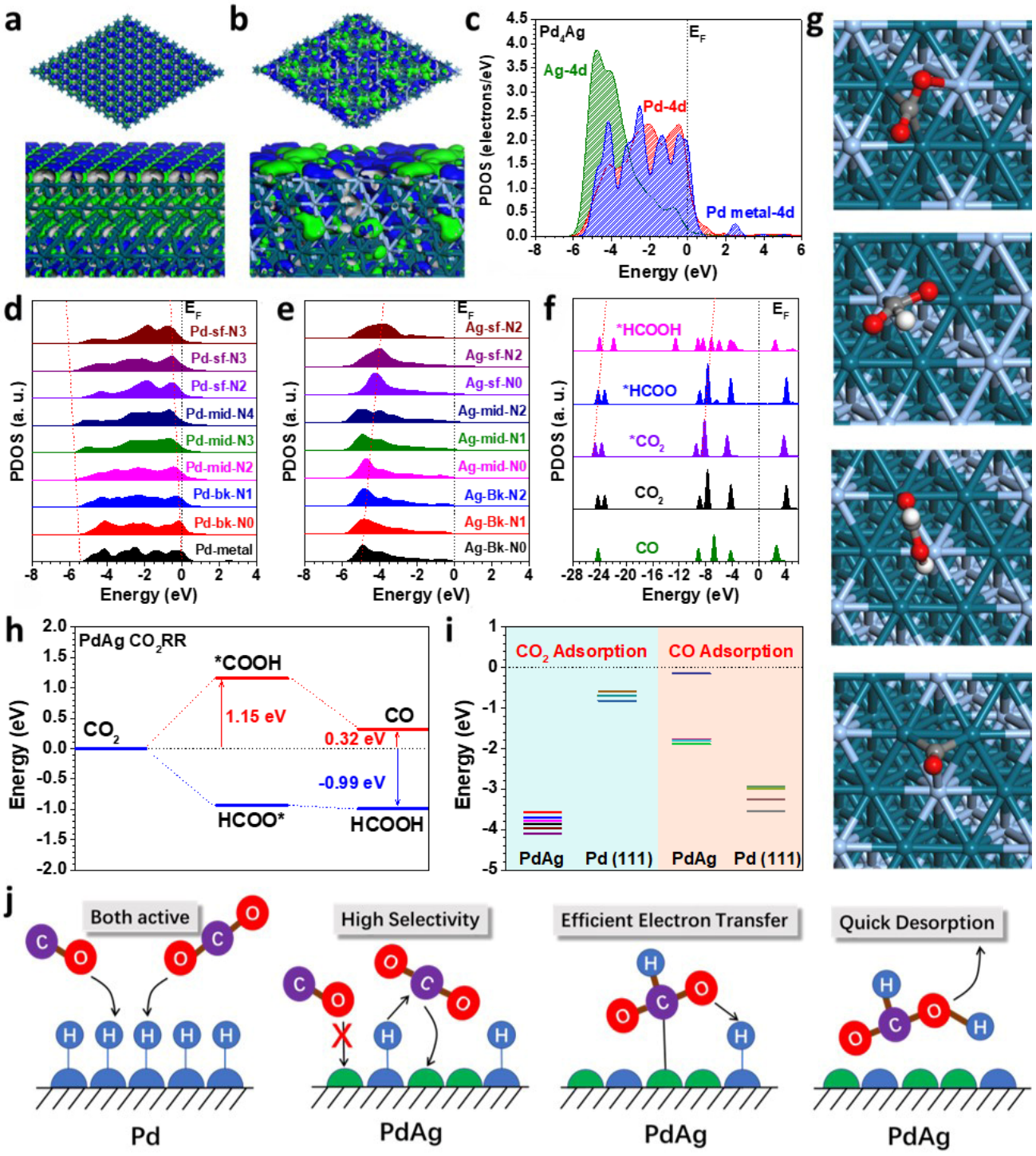

Figure 4. The lattice structure and electronic distribution near E_F of (a) Pd (111) surface and (b) PdAg. (c) The PDOS of Pd_4Ag. (d) The site-dependent PDOS of Pd-4d orbitals in Pd_4Ag. (e) The site-dependent PDOSs of Ag-4d orbitals in Pd_4Ag. (f) The PDOS of key intermediates during the formation of formate in CO_2RR. (g) The lattice structure of the key intermediate adsorption on the Pd_4Ag surface. (h) The energetic reaction ways of CO_2RR on Pd_4Ag. (i) The adsorption energies comparison between Pd_4Ag and Pd (111) surfaces. (j) The schematic diagram of the anti-poisoning mechanism of Pd_4Ag.